Mathematical Medicine and Biology Page 1 of 25
doi:10.1093/imammb/dqnxxx

Mathematical modelling of blood–brain barrier failure and edema

GEORGINA E. LANG, DOMINIC VELLA, SARAH L. WATERS AND ALAIN GORIELY
Mathematical Institute, University of Oxford,
Oxford, OX2 6GG, UK.

[Received on 23 February 2016]

Injuries such as traumatic brain injury and stroke can result in increased blood–brain barrier permeability. This increase may lead to water accumulation in the brain tissue resulting in vasogenic edema. Although the initial injury may be localised, the resulting edema causes mechanical damage and compression of the vasculature beyond the original injury site. We employ a biphasic mixture model to investigate the consequences of blood–brain barrier permeability changes within a region of brain tissue and the onset of vasogenic edema. We find that such localised changes can indeed result in brain tissue swelling and suggest that the type of damage that results (stress damage or strain damage) depends on the ability of the brain to clear edema fluid.

Keywords:
Blood–brain barrier biphasic model brain mechanics vasogenic edema mathematical modelling

1. Introduction

Brain cells are sensitive to changes in the chemical composition of their surroundings; the interaction between the blood, whose composition will inevitably vary over time, and the brain must therefore be carefully regulated. This regulation is achieved by the presence of a protective layer (the 'blood–brain barrier' or BBB), which consists of a continuous layer of endothelial cells and membranes (Abbott et al., 2006). Substances within the blood (such as ions and proteins) cannot pass between endothelial cells due to the tight junctions between adjacent cells. Water, some gases and lipid-soluble molecules pass through the BBB by passive diffusion, while glucose and some larger molecules (e.g. amino acids) are selectively transported. In this way, the composition of the interstitial fluid between brain cells remains well-controlled despite the inevitable fluctuations in the concentration of substances in the blood (Abbott et al., 2010).

Nevertheless, the balance remains a delicate one: an increase in the permeability of the blood–brain barrier by the loosening of the tight junctions allows fluid (and other substances) to move more easily from capillaries into the tissue interstitium. This may, in turn, lead to water accumulation and swelling, or edema (*e.g.* Simard et al., 2007; Kimelberg, 1995). Edema caused by disruption of the BBB is referred to as vasogenic edema (though other types of edema exist, as discussed by Goriely et al., 2015, for example) and is a serious consequence of head injuries that leads to lasting damage, if not death.

We use a mathematical model of soft biphasic tissue, to investigate the effect of an increase in BBB permeability to water on the swelling of brain tissue. It has been reported that localized edema can exacerbate the original injury by spreading: mechanical deformation due to edema leads to compression of blood vessels, and raised intracranial pressure in the previously healthy tissue surrounding the original injury site (Walberer et al., 2008; Flechsenhar et al., 2013). We are particularly interested in understand-

[1]Email: goriely@maths.ox.ac.uk

ing how a locally damaged region, with increased BBB permeability, can cause further damage to the surrounding tissue.

This paper is structured as follows. In §1.1, we discuss fluid transport in the healthy brain, and the changes that occur following injury. As we are interested in understanding how a locally swollen region affects the surrounding tissue, §1.2 concerns the mechanisms by which mechanical changes can cause damage to previously healthy tissue. In §2 we present the biphasic modelling approach that we use to couple transvascular fluid flux with a biphasic model for soft tissues. We consider a spherically symmetric geometry, since this is the simplest geometry that allows us to investigate the effect of a local region of increased BBB permeability. In §4 we present solutions of the model, focussing particularly on the stresses and strains generated in the tissue. In Appendix A we discuss how the timescales predicted by the model compare with those observed in practice for the evolution of edema, while Appendix B compares the results of infinitesimal and finite deformation elasticity.

1.1 *Fluid transport in the brain*

The brain has four fluid compartments: cerebrospinal fluid (CSF), interstitial fluid (ISF), intracellular fluids, and the blood vasculature (Ek et al., 2005). A unique feature of the brain vasculature is that all the arterioles, capillaries, and venules within the brain parenchyma are surrounded by astrocytic endfeet: these endfeet contain Aquaporin 4 (AQP4) water channels which play a key role in fluid transport. Additionally, these endfeet create the outer wall of an annular perivascular space. It has been postulated that this perivascular space provides a low-resistance pathway for the flow of CSF from the subarachnoid space, driven by CSF gradients in addition to arterial pulsatility (among other factors). There is now evidence that there is continuous exchange between the CSF and ISF fluid compartments, with the exchange dependent on the local hydrostatic and osmotic pressure gradients (Rapoport, 1997). Furthermore, it has been postulated that the aforementioned perivascular spaces aids in the continuous mixing of CSF and ISF, with the AQP4 channels in the astrocytic endfeet of the BBB allowing CSF/ISF exchange deep within the brain parenchyma (Jessen et al., 2015). The ISF is then collected in the perivenous space from where it drains out of the brain (Jessen et al., 2015; Louveau et al., 2015; Bakker et al., 2016). In this healthy state, the rate of bulk flow of ISF has been reported to lie in the range 0.15-0.29 μl/min per gram of brain tissue in the rat and rabbit; it is believed to have a similar average value in humans (Abbott, 2004).

When brain tissue is damaged, the structure and function of the BBB may be impaired, *e.g.* due to alterations to the AQP4 water channels, leading to an increase in the permeability of the BBB to fluid and plasma products (Bakker et al., 2016; Unterberg et al., 2004). This change allows water to move more easily into the damaged region of tissue, causing an accumulation of fluid within the tissue (edema). Pressure gradients develop in the tissue (with the pressure decreasing with distance from the damaged regions), and edema can spread as fluid permeates through the brain tissue down these pressure gradients (Reulen et al., 1977). The total amount of swelling reaches a maximum (maximal edema) at least 6 hours (and up to 3 days) after the initial injury in rats (Hatashita et al., 1988), whilst monitoring of hospital patients indicates that maximal edema occurs 3-5 days after injury in humans (Marmarou et al., 2000).

An increase in BBB permeability is not the only cause of edema (Simard et al., 2007). Changes in tissue osmolarity are observed in the swollen brain tissue, and it is thought that these changes in osmotic gradients within the tissue also drive fluid accumulation (Hatashita et al., 1988; Kawamata et al., 2007). Whilst it is evident that osmotic changes occur when brain tissue swells, we neglect osmotic effects here and focus on the consequences of changes in BBB permeability for brain tissue swelling. Osmotic

changes due to hypoxia, and the resulting propagation of damage, have been considered by Lang et al. (2015).

1.2 *Consequences of edema*

We consider two mechanical mechanisms through which local edema can cause further damage to the surrounding tissue. The first mechanism we investigate is axonal stretch. Axons are the protrusions of neurons, which carry chemical signals through the brain. Axons can be damaged by mechanical deformation, with the severity of the damage caused depending upon both the rate and the magnitude of the imposed strain (Smith and Meaney, 2000). It has been shown that rapid deformations are particularly damaging. For example, Tang-Schomer et al. (2010) showed that stretching isolated axons at strain rates of 44 s^{-1} caused mechanical failure of the axons. While such rapid strain rates may be encountered in impacts, edema evolves over a relatively slow time scale. We shall therefore assume in our model that it is the magnitude of the applied strain, and not the rate of strain, that causes damage.

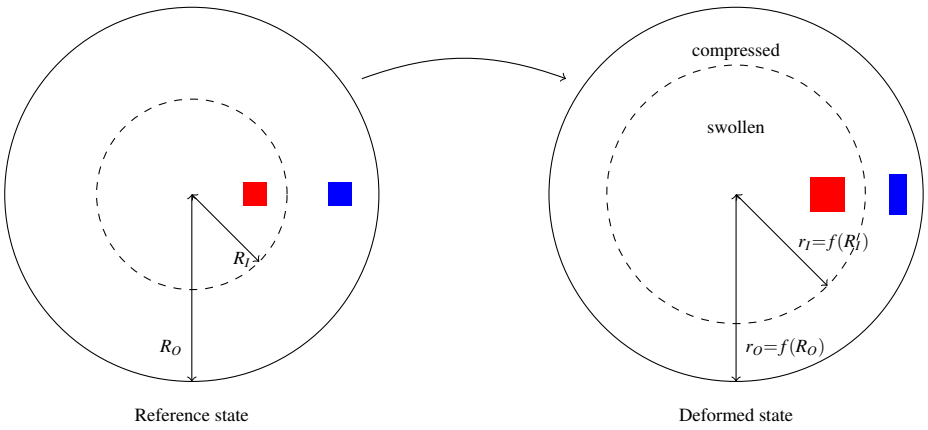

FIG. 1. Schematic illustrating how localised swelling within a confined region can result in both stretch and compression of tissue. The coloured regions show how a region that is square in the reference state may become expanded in both the circumferential and radial directions if swollen, but may expand in one direction and compress in the other if squeezed.

If a small region of brain tissue swells, then, because of the constriction imposed by the presence of the skull, and assuming that the tissue is saturated so that there are no voids, we expect other regions of the tissue to be compressed and stretched (in particular, compression in one direction can cause stretching in another, see Figure 1). The second mechanism of tissue damage is due to the mechanical stress within the tissue. Increased intracranial pressure (ICP) is detrimental because it can cause compression of the vascular network (Dunn, 2002; Steiner and Andrews, 2006). If the brain suffers from reduced blood flow (ischemia) as a result of this compression then the tissue may become hypoxic (reduced oxygen level), ultimately leading to cell damage and death. The actual relationship between cerebral blood flow and intracranial pressure is complicated, because the brain is able to autoregulate its blood flow over a range of ICPs (by dilating or contracting the arteries that bring blood to the brain (Strandgaard et al., 1973)). This autoregulation mechanism is difficult to quantify, and it is unclear whether this process could maintain blood flow locally if just a small region of the brain were damaged. We therefore

simply postulate that compression of capillaries may lead to tissue damage.

In summary, we will consider two simple measures of 'damage' in our modelling. The first is 'strain damage', which is detrimental to brain tissue because it causes damage to axons (hence preventing the brain from functioning). The potential for strain damage will be tracked using the extension of the tissue mixture. The second is 'stress damage', which represents the extent to which the swollen tissue will exert a compressive force on capillaries (leading to hypoxia and subsequent cell death). The potential for stress damage will be tracked via the compressive stress within the mixture. Note that the distinction between stress and strain damage here is important as large compressive stresses can be produced with small strains because of incompressibility. Note that the level of compressive stress that leads to cell damage or the level of stretch that leads to axonal damage have not been properly quantified in brain tissue. Therefore, we use these metrics as qualitative descriptors of the potential for tissue damage rather than as quantitative predictors of when and where damage actually occurs. We also comment that tissue damage is understood here as any mechanical change that affects the proper biological function or integrity of the tissue rather than changes in the microstructure that accumulate over time until failure as found in classical damage mechanics. The two notions are closely related, yet a proper connection remains elusive.

1.3 *Mathematical modelling approach*

As we are interested in understanding the relationships between water accumulation (edema), stress, and strain within the tissue, we use a biphasic mixture approach (Nagashima et al., 1990b; Wilson et al., 2005). Brain tissue is treated as a mixture of solid and fluid phases, and a diffuse source term is incorporated throughout the mixture to represent transvascular fluid flux entering the brain tissue from capillaries.

To our knowledge, the work of Nagashima et al. (1990a,b) is the only attempt to apply this modelling approach to vasogenic edema. They used a realistic two-dimensional brain geometry (based upon a coronal segment of a cat brain), and increased the hydraulic conductivity of the BBB locally to simulate BBB damage. However, their choice of boundary conditions and parameter values is not consistent with current literature. For example, Nagashima et al. (1990b) imposed a no fluid flux boundary condition between the tissue and SAS, contradicting more recent understanding of fluid flow in the brain (Redzic et al., 2005). Furthermore, they used a Young's modulus of $E \approx 10^4$ Pa while recent experiments suggest that $E \approx 600$ Pa is more appropriate (Taylor and Miller, 2004).

A similar biphasic approach has been applied to model fluid infusion into brain tissue and hydrocephalus. However, the majority of authors in this related area neglect transvascular fluid flux (for example Chen and Sarntinoranont, 2007; Smillie et al., 2005; Wirth and Sobey, 2009), which is the source of excess fluid in vasogenic edema. Smith and Humphrey (2007) incorporate transvascular fluid flux to investigate the effect of a brain tumour on infusion, motivated by the fact that the BBB is more permeable in tumour than healthy tissue. They used a spherically symmetric model, similar to the geometry studied here. However, they were primarily interested in understanding profiles of the fluid flux within the brain tissue (with application to advective drug delivery), rather than deformations of, and compressive stresses within, the brain tissue itself.

We also note that all of the models mentioned above use a version of the biphasic theory that is valid only for infinitesimally small strains. However, experimental studies (see for example Simard et al. (2007) and Walberer et al. (2008)) suggest that brain tissue undergoes relatively large deformations when it swells. We therefore develop a finite-deformation framework, comparing the results of finite and infinitesimal deformation models in Appendix B to show that the infinitesimal theory provides good

insight into the swelling process.

Finally, we note that models going beyond the biphasic approach exist, including multiple network poroelastic models in which the capillaries are explicitly modelled as a further fluid network in addition to the interstitial fluid (Tully and Ventikos, 2011). However, this approach leads to a more complex set of governing equations, and introduces parameters that are difficult to quantify from experimental data. Here, therefore, we do not explicitly consider fluid flow through the vasculature, focussing instead on deformations and pressure changes within the tissue itself.

2. Biphasic model for tissue damage

We now discuss the governing equations, geometry, and physiological parameter values appropriate to our model. We follow the biphasic modelling approach of Nagashima et al. (1990b) and Smith and Humphrey (2007).

2.1 *Governing equations*

Brain tissue is modelled as a saturated biphasic mixture of two inherently incompressible phases: a hyperelastic solid phase 's' and fluid phase 'w' (see García and Smith, 2010; Holmes, 1985; Mak et al., 1987, for example). We note that, unless the solid phase fully occupies a given region, its volume can change by changing the pore size (much like squeezing a sponge) even while the solid and liquid phases remain incompressible. Therefore, when phases mix, local conservation of volume is not guaranteed and we assume that the mixture is compressible in order for the conditions of saturation and fixed total volume (volume enclosed by the skull) to be satisfied. Definitions of variables in the biphasic model are given in Table 1. The tissue is described in the reference (Lagrangian) configuration by the material coordinates $\mathbf{X}$, and, after deformation, is described by new (Eulerian) coordinates $\mathbf{x} = \boldsymbol{\chi}(\mathbf{X}, t)$ (referred to as the current configuration), where t denotes time. The tissue displacement $\mathbf{u}$ is given by the change in position,

$$\mathbf{u} = \mathbf{x} - \mathbf{X}, \tag{2.1}$$

and the deformation gradient tensor $\mathbf{F}$ is defined as,

$$\mathbf{F} = \frac{\partial \boldsymbol{\chi}}{\partial \mathbf{X}} = \mathbf{I} + \frac{\partial \mathbf{u}}{\partial \mathbf{X}}. \tag{2.2}$$

We shall also make repeated use of the dilation, $J = \det(\mathbf{F})$, which is the change in volume due to deformation.

ϕ^s (ϕ^w)	Volume fraction of solid (fluid)
$\mathbf{v}^s$ ($\mathbf{v}^w$)	Velocity of solid (fluid)
p	Pore pressure
$\mathbf{u}$	Solid displacement
$\boldsymbol{\sigma}_e$	Effective mixture stress
Q	Volumetric fluid source

Table 1. Definition of variables in the biphasic model.

We assume the mixture is saturated so that,

$$1 = \phi^s + \phi^w. \tag{2.3}$$

To allow for transvascular water flux from capillaries into tissue, we incorporate a fluid source, denoted by Q. The mass of the solid and fluid phases is conserved:

$$0 = \frac{\partial \phi^s}{\partial t} + \nabla \cdot (\mathbf{v}^s \phi^s), \tag{2.4}$$

$$Q = \frac{\partial \phi^w}{\partial t} + \nabla \cdot (\mathbf{v}^w \phi^w). \tag{2.5}$$

where Q (s^{-1}) is the source strength (the local source volume of fluid added per volume of tissue per unit time). A constitutive form for the fluid source term Q is discussed in §2.2. Note that since each phase is inherently incompressible, then to accommodate a source of fluid in the model (Q in Equation (2.5)), fluid must exit the domain (see discussion of boundary conditions).

The movement of the fluid phase is driven by pressure gradients according to Darcy's law,

$$\phi^w(\mathbf{v}^w - \mathbf{v}^s) = -K\nabla p, \tag{2.6}$$

where $K = k/\eta$ with k (m^2) the intrinsic permeability of the mixture and η (Pa s) the dynamic viscosity of the interstitial liquid; we refer to the combination K as 'the permeability of the mixture to the interstitial liquid'.

Using the mass conservation equations (2.4, 2.5), the saturation condition (2.3), and Darcy's law (2.6), allows the volume fractions ϕ^w, ϕ^s and fluid velocity $\mathbf{v}^w$ to be eliminated. This yields a single equation for mass conservation within the mixture:

$$\nabla \cdot \mathbf{v}^s - \nabla \cdot (K\nabla p) = Q. \tag{2.7}$$

Since the solid phase is inherently incompressible, mass conservation of the solid phase (2.4) can equivalently be written in terms of the deformation. We find that

$$\phi^s = \frac{\phi^s_{(0)}}{J}, \tag{2.8}$$

where $\phi^s_{(0)}$ is the volume fraction of the solid in a stress-free reference state. By taking the partial derivative of equation (2.8) with respect to time, it can be shown that equation (2.4) and equation (2.8) are equivalent.

The mixture Cauchy stress $\boldsymbol{\sigma}$ is divided into two components so that,

$$\boldsymbol{\sigma} = \boldsymbol{\sigma}_e - p\mathbf{I}, \tag{2.9}$$

where the effective Cauchy stress $\boldsymbol{\sigma}_e$ represents the elastic component of the stress and p is the pore pressure. In large deformation, the effective Cauchy stress is obtained from a strain-energy function $W(\boldsymbol{F})$ by

$$\boldsymbol{\sigma}_e = \frac{1}{J}\boldsymbol{F} \cdot \frac{\partial W}{\partial \boldsymbol{F}}. \tag{2.10}$$

Note that any rearrangement of tissue components due to a change in fluid content would result in a deformation of the solid phase, and that the stress associated with this is captured by this constitutive relationship.

Several strain-energy functions have been utilised in the literature to represent brain tissue (Moran et al., 2014). For example, an Ogden-type hyperelastic model was applied to brain tissue by García and Smith (2009) to model infusion tests, whilst the Fung model was used by Elkin et al. (2010) and Lang et al. (2014) to model the equilibrium behaviour of brain tissue slices in solution baths of differing concentrations. Lang (2014) investigated the behaviour of several strain-energy functions and showed that for moderate homogeneous swelling (bulk volume changes of up to 50%), the neo-Hookean, Fung and Ogden models all show quantitatively similar behaviour for parameters relevant to the brain. Therefore, for simplicity we consider here a compressible neo-Hookean strain-energy function of the form

$$W = \frac{\mu_s}{2}\left(\lambda_1^2+\lambda_2^2+\lambda_3^2-3-2\log J\right)+\frac{\lambda_s}{2}(J-1)^2 \tag{2.11}$$

in which $\lambda_{1,2,3}$ represent the principal stretches (the eigenvalues of $\boldsymbol{F}^{\mathrm{T}}\boldsymbol{F}$) and λ_s and μ_s can be identified with the Lamé coefficients for small deformations.

In Appendix B we also consider the case of small deformations, in which case, the stress tensor may be written

$$\boldsymbol{\sigma}_e = \lambda_s \mathrm{tr}(\mathbf{e})\mathbf{I}+2\mu_s\mathbf{e}, \tag{2.12}$$

with $\mathbf{e} = [\nabla\mathbf{u}+(\nabla\mathbf{u})^T]/2$ the linear strain tensor.

Neglecting inertia and assuming no body forces, the mixture stress is divergence free,

$$\nabla\cdot(\boldsymbol{\sigma}_e - p\mathbf{I}) = \mathbf{0}. \tag{2.13}$$

Finally the velocity of the solid phase is related to the solid displacement through

$$\mathbf{v}^s = \left.\frac{\partial\mathbf{u}}{\partial t}\right|_{\mathbf{X}}, \tag{2.14}$$

where the right-hand side is the convective derivative over time of displacement. Along with appropriate boundary and initial conditions, equations (2.7) and (2.13) constitute two equations for two unknowns: $\mathbf{u}$ (solid displacement) and p (pore pressure). The solid velocity $\mathbf{v}^s$, featuring in equation (2.7), is related to $\mathbf{u}$ by equation (2.14) and the effective Cauchy stress $\boldsymbol{\sigma}_e$, featuring in equation (2.13), is related to $\mathbf{u}$ by equations (2.2) and (2.10). However the form of the source strength Q requires some discussion and we turn to this now.

2.2 *Starling's law for transcapillary fluid exchange*

The rate of water movement, Q, across the blood–brain barrier from capillaries into the tissue is dependent upon the hydrostatic and osmotic pressure differences between the plasma and interstitial fluid. Starling's law is typically used to model flux across a capillary wall (Rapoport, 1997; Korthuis et al., 2010):

$$Q = L_p\left[\Delta p - \sigma_{\mathrm{ions}}\Delta\Pi_{\mathrm{ions}} - \sigma_{\mathrm{oncotic}}\Delta\Pi_{\mathrm{oncotic}}\right], \tag{2.15}$$

where L_p ($\mathrm{Pa}^{-1}\mathrm{s}^{-1}$) is the capillary hydraulic conductivity (which physically represents the volumetric flow rate across from the capillary network into the tissue, per unit volume of tissue per unit pressure

difference), $\Delta p = p_{\text{cap}} - p$ is the hydrostatic pressure jump across the capillary wall (with p_{cap} the capillary pressure), and $\Delta\Pi_{\text{ions}}$, $\Delta\Pi_{\text{oncotic}}$ are the osmotic pressure differences due to ions and proteins, respectively. The reflection coefficients σ_{oncotic} and σ_{ions} represent the permeability of the capillary wall to a solute (a reflection coefficient of 1 means that the wall is totally impermeable to the particular solute, whilst a reflection coefficient of 0 means that the wall is totally permeable and hence that osmotic pressure does not lead to flow).

We neglect changes in solute concentration in the tissue, and assume that the osmotic pressures and reflection coefficients, along with capillary pressure, can be incorporated into a single constant parameter Y. Then,

$$Q = L_p\,[Y - p]\,, \tag{2.16}$$

where $Y := p_{\text{cap}} - [\sigma_{\text{ions}}\Delta p_{\text{ions}} + \sigma_{\text{oncotic}}\Delta p_{\text{oncotic}}]$ (Pa) is the driving pressure for fluid flow across the capillary wall, and p is the pore pressure in the tissue.

Substituting the Starling capillary source term (2.16) into the mass conservation equation (2.7) gives

$$\nabla\cdot\mathbf{v}^s - \nabla\cdot(K\nabla p) = L_p(Y-p). \tag{2.17}$$

The parameters in this equation, the capillary hydraulic conductivity L_p, driving pressure Y and tissue Darcy permeability K, could be taken to be constants, or functions of other variables in the system. For example, spatial dependence could be used to represent material heterogeneities, or the tissue permeability K could be made deformation dependent (see Sobey et al., 2012; Wirth and Sobey, 2006, for example). For simplicity, we assume that Y and K are constant throughout the tissue; however, we allow L_p to be a function of position to simulate local damage to the BBB.

2.3 *Geometry and boundary conditions*

The system (2.13) and (2.17) must be considered together with appropriate initial and boundary conditions. In this main text we consider only the steady-state problem and so consider only the appropriate boundary conditions. In Appendix A we consider the role of dynamics and so discuss appropriate initial conditions there.

We consider a spherically symmetric brain, of radius H, that undergoes spherically symmetric deformations. Then the current ($\mathbf{x} = r\hat{\mathbf{e}}_{\mathbf{r}}$) and reference ($\mathbf{X} = R\hat{\mathbf{e}}_{\mathbf{R}}$) configurations are related by $r = f(R)$ (so that $f(R) = R$ everywhere means that the tissue is undeformed). Then the deformation gradient tensor, (2.2), and dilation are,

$$\mathbf{F} = \nabla_{\mathbf{X}}\mathbf{x} = \begin{pmatrix} f' & 0 & 0 \\ 0 & \dfrac{f}{R} & 0 \\ 0 & 0 & \dfrac{f}{R} \end{pmatrix}, \qquad J = \det(\mathbf{F}) = \frac{f^2 f'}{R^2}, \tag{2.18}$$

where primes denote differentiation with respect to R. The radial displacement is related to the deformation by $u(R) = f(R) - R$. The variables of interest are the pore pressure $p(R)$ and the radial deformation $f(R)$, which are found as the solution of the governing equations (2.13) and (2.17). The BBB hydraulic conductivity L_p is taken to be a function of R, to allow the BBB to be increased locally to mimic regional damage.

As L_p depends upon R, it is natural to work in the Lagrangian frame. We rewrite the governing equations in Lagrangian coordinates and solve the resulting equation in the reference domain. To

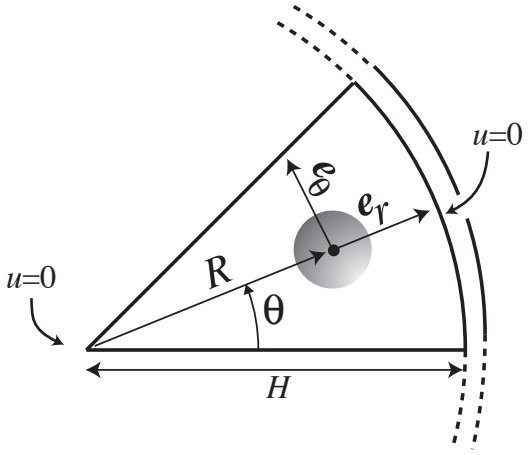

FIG. 2. Geometric setup. We assume a spherical symmetry. The radial coordinates and the associated basis are shown. At $R = 0$ and $R = H$, we assume a no-displacement condition.

rewrite the mass balance (2.17) in Lagrangian coordinates, we use the relations between the Eulerian and Lagrangian description of the gradient of a scalar field and divergence of a vector field,

$$\nabla_{\mathbf{x}}\phi = \mathbf{F}^{-T}\nabla_{\mathbf{X}}\phi, \qquad \nabla_{\mathbf{x}}\cdot\mathbf{g} = \frac{1}{J}\nabla_{\mathbf{X}}\cdot\left(J\mathbf{F}^{-1}\mathbf{g}\right), \tag{2.19}$$

where $\phi(\mathbf{x})$ and $\mathbf{g}(\mathbf{x})$ are arbitrary scalar and vector functions respectively (Ogden, 1984). Hence we rewrite the mass conservation equation (2.17), as

$$\frac{1}{J}\nabla_{\mathbf{X}}\cdot\left(J\left(\mathbf{F}^{-1}\mathbf{v}^s - \mathbf{F}^{-T}\mathbf{F}^{-1}K\left(\nabla_{\mathbf{X}}p\right)\right)\right) = L_p(Y-p). \tag{2.20}$$

The stress balance is easily reformulated into a Lagrangian frame momentum equation, so that

$$\nabla_{\mathbf{X}}\cdot\left(\mathbf{S}_e - pJ\mathbf{F}^{-T}\right) = 0, \tag{2.21}$$

where $\mathbf{S}_e = J\boldsymbol{\sigma}_e\mathbf{F}^{-T}$ is the effective first Piola-Kirchhoff stress.

For the boundary conditions, we apply symmetry conditions at the origin

$$\left.\frac{\mathrm{d}p}{\mathrm{d}R}\right|_{R=0} = 0, \qquad u|_{R=0} = 0. \tag{2.22}$$

We consider an idealised geometry representing the brain as shown in Figure 2. To capture the effect of the skull and other brain structures, we impose no displacement at the outer surface, $R = H$,

$$u|_{R=H} = 0, \tag{2.23}$$

and a pressure dependent flux,

$$-K\frac{1}{f'}\left.\frac{\partial p}{\partial R}\right|_{R=H} = \Gamma\, p|_{R=H}, \tag{2.24}$$

where Γ is a parameter representing the ability of a fluid to be cleared from the brain. This flux condition captures the observation that fluid drainage from the brain into the venous system occurs at a rate proportional to the pressure difference between brain and venous blood (Johanson, 2008). The left hand side of equation (2.24) comes from rewriting the fluid flux given by Darcy's law, equation (2.6), in Lagrangian coordinates, using (2.18) and (2.19a).

When considering a similar geometric set up to model an infusion test, other authors (eg. Chen and Sarntinoranont, 2007; Smith and Humphrey, 2007) set $u = 0$, $p = 0$ on the outer boundary. This boundary condition models a scenario in which the outer boundary is sufficiently far from the infusion site that it is not affected by the infusion, and it is not clear whether this assumption would be appropriate to edema. However, in the limit of large Γ, (2.24) becomes equivalent to $p = 0$. Here, we use the more general condition (2.24) to investigate how the pressure at the outer edge of the brain is affected by the damage at the centre.

3. Determination of key parameters

3.1 *Non-dimensionalisation*

We non-dimensionalise the governing equations (2.21), (2.14) and (2.20), along with the boundary conditions (2.22) and (2.23)–(2.24) by letting

$$\mathbf{x} = H\bar{\mathbf{x}}, \qquad t = \frac{H^2}{K(\lambda_s + 2\mu_s)}\bar{t}, \qquad p = (\lambda_s + 2\mu_s)\bar{p}, \tag{3.1}$$

$$\mathbf{u} = H\bar{\mathbf{u}}, \qquad \mathbf{v}^s = \frac{K(\lambda_s + 2\mu_s)}{H}\bar{\mathbf{v}}^{\mathbf{s}}, \tag{3.2}$$

where we use bars to denote dimensionless variables.

The dimensionless Piola-Kirchhoff and Cauchy stress tensors are defined as $\bar{\mathbf{S}}_e = \mathbf{S}_e/(\lambda_s+2\mu_s)$ and $\bar{\boldsymbol{\sigma}}_e = \boldsymbol{\sigma}_e/(\lambda_s+2\mu_s)$ respectively, and we define the dimensionless parameters,

$$\bar{\lambda}_s = \frac{\lambda_s}{(\lambda_s+2\mu_s)}, \qquad \bar{\mu}_s = \frac{\mu_s}{(\lambda_s+2\mu_s)}, \qquad \bar{L}_p = \frac{L_p H^2}{K}, \tag{3.3}$$

$$\bar{Y} = \frac{Y}{(\lambda_s+2\mu_s)}, \qquad \bar{\Gamma} = \frac{\Gamma H}{K}. \tag{3.4}$$

We choose the $\lambda_s + 2\mu_s$ as a natural pressure scale; by this choice the dimensionless elastic parameters $\bar{\lambda}_s$, $\bar{\mu}_s$ are of order 1. Time has been scaled using the poroelastic consolidation time scale. Then (dropping bars from the dimensionless variables, but keeping them on the dimensionless parameters) the mass conservation and momentum balance governing equations may be rewritten,

$$\frac{1}{J}\nabla_{\mathbf{X}} \cdot \left[J\mathbf{F}^{-1}\mathbf{v}^s - J\mathbf{F}^{-T}\mathbf{F}^{-1}\left(\nabla_{\mathbf{X}} p\right)\right] = \bar{L}_p(\bar{Y} - p), \tag{3.5}$$

$$\nabla_{\mathbf{X}} \cdot \mathbf{S}_e = \nabla_{\mathbf{X}}\left(pJ\mathbf{F}^{-T}\right), \tag{3.6}$$

along with equation (2.14) (relating solid velocity and displacement rate), which remains unchanged.

The symmetry boundary conditions at the origin (2.22) remain unchanged, whilst on the outer boundary (2.23) and (2.24) become

$$u|_{R=1} = 0, \qquad -\frac{1}{f'}\frac{\partial p}{\partial R}\bigg|_{R=1} = \bar{\Gamma}\, p|_{R=1}. \tag{3.7}$$

Dimensional			Dimensionless	
H	Typical radius	1cm	-	-
L_p	Capillary hydraulic permeability		$\bar{L}_p = L_p H^2/K$	
	Healthy:	$10^{-9}-10^{-8}$ Pa^{-1}s^{-1}		0.1-1
	Damaged:	$10^{-7}-10^{-6}$ Pa^{-1}s^{-1}		10-100
K	Tissue Darcy permeability	$10^{-12}-10^{-11}$ m^{2}Pa^{-1}s^{-1}	-	-
μ_s, λ_s	Elastic parameters	216, 505 Pa	$\bar{\mu}_s = \mu_s/(\lambda_s+2\mu_s)$, $\bar{\lambda}_s = \lambda_s/(\lambda_s+2\mu_s)$	0.25, 0.5
Y	Transvascular driving pressure	1000 Pa	$\bar{Y} = Y/(\lambda_s+2\mu_s)$	1
Γ	Permeability of the tissue boundary	††	$\bar{\Gamma} = \Gamma H/K$	††

†All pressures are given relative to the healthy SAS pressure

††The appropriate value to use for the permeability of the brain boundary is unknown. We consider a range of values for this parameter $\bar{\Gamma}$ in §4.2

Table 2. Summary of the dimensional parameters for the biphasic model of the brain. These values are discussed in Section 3.2. Throughout we take $H = 1$ cm as the typical radius of our spherical domain.

Aside from the $O(1)$ dimensionless Lamé coefficients $\bar{\lambda}_s$ and $\bar{\mu}_s$, our problem contains three dimensionless groups: $\bar{L}_p$, $\bar{Y}$ and $\bar{\Gamma}$. Physically, $\bar{L}_p$ represents the ratio of the ease with which fluid can flow out from capillaries into tissue, versus the ease with which fluid can drain through the tissue over a distance H. Thus $\bar{L}_p \gg 1$ means that fluid can enter the tissue more easily than drain out, whilst $\bar{L}_p \ll 1$ means that fluid can drain out of the tissue more easily than it enters. The parameter $\bar{Y}$ is the dimensionless driving pressure for transcapillary water movement. Finally, $\bar{\Gamma}$ represents the relative ease with which fluid can flow out through the brain boundary, compared with the ease with which it flows a distance H through the brain.

In §4 we shall investigate solutions to the model (3.5)-(3.7). However, first we discuss physiological parameter values relevant to this model.

3.2 *Physiological parameter values*

Throughout we take $H = 1$ cm as the typical radius of our spherical domain, which corresponds to the typical size of a small mammal brain used in experimental studies (Neal et al., 2007). The elastic properties and permeability of brain tissue have been extensively investigated in the literature. The permeability of brain tissue to water, K, is consistently found to be of order $10^{-12} - 10^{-11}$ m^{2}Pa^{-1}s^{-1} (Chen and Sarntinoranont, 2007; Smillie et al., 2005). For quasi-static deformations, the Lamé coefficients of brain tissue are $\mu_s \approx 216$ Pa, $\lambda_s \approx 505$ Pa (Taylor and Miller, 2004).

There is less discussion in the literature of the capillary hydraulic conductivity L_p; we therefore consider this parameter in more depth. Recall that the hydraulic conductivity L_p (Pa^{-1}s^{-1}) can be interpreted as the volumetric flow rate from the capillary network into the tissue, per unit volume of tissue per unit pressure difference. In a compartment model of the brain, Rapoport (1978) used 1.5×10^{-4} cm^{3}mmHg^{-1}s^{-1} as a bulk hydraulic conductivity for the entire brain. Physically, this corresponds to the volumetric flow rate from the capillary network into the tissue per unit pressure difference, for the entire brain (*i.e.* not per unit volume of tissue). To convert their value into our units, we divide by the brain volume: based upon a typical brain volume of 1500 cm^3 this yields $L_p = 1 \times 10^{-7}$ mmHg^{-1}s^{-1}. Bradbury (1985) summarised experimental results from the literature, noting that a value of $0.8 - 1.5 \times 10^{-9}$ cm s^{-1}mmH$_2$O^{-1} had been found for the hydraulic conductivity per surface area of capillary. The typical capillary surface area per volume of brain tissue is $100 - 150$ cm^{2}g^{-1} in grey matter and one third that in white matter (Smith, 2003). Thus from the values given by Bradbury (1985) we can estimate $L_p = 1-3 \times 10^{-6}$ mmHg^{-1}s^{-1} in grey matter and $L_p = 3 - 10 \times 10^{-7}$ mmHg^{-1}s^{-1} in white matter (since 1 mmHg = 13.6 mmH$_2$O). As these two approaches yield similar estimates for the capillary hydraulic permeability of healthy tissue, we take

$L_p = 10^{-7}-10^{-6}$ mmHg^{-1}s^{-1} (equivalent to $10^{-9}-10^{-8}$ Pa^{-1}s^{-1}). In damaged brain tissue, the capillary hydraulic permeability increases at least 100-fold (Rapoport, 1978).

The transvascular driving pressure Y was defined as the capillary pressure less the osmotic pressure difference between the blood and the interstitial fluid. We use the parameter values reported by Rapoport (1997), but note that there is considerable uncertainty regarding this parameter (for example, the capillary pressure may not be constant in space). According to Rapoport (1997), the capillary pressure is 32 mmHg greater than brain tissue pressure, and the osmotic pressure difference across the BBB is 25 mmHg. Thus the transvascular driving pressure is 7 mmHg (approximately 1000 Pa).

The value of Γ, the permeability of the tissue boundary, is unknown. We will therefore investigate a range of values of Γ in the following sections.

3.3 *Key parameters*

In Appendix A, we show that the dimensionless parameter $\bar{L}_p = L_p H^2/K$ is important in determining the behaviour of the system. Dimensional analysis of the model suggests that when $\bar{L}_p \ll 1$ the pore pressure in the tissue remains low, whilst when $\bar{L}_p \gg 1$ the pore pressure can increase up to the capillary driving pressure $\bar{Y}$. Interestingly, our parametrisation (see Table 2) suggests that $\bar{L}_p > 1$ in damaged tissue and $\bar{L}_p < 1$ in healthy tissue. This suggests that an increase in capillary permeability might be expected to lead to significant pressure changes in the tissue.

Also in Appendix A we investigate the timescales over which this biphasic system evolves. We show that when $\bar{L}_p \geqslant 1$ the system evolves over the dimensional time scale $t \sim H^2/K/(\lambda_s + 2\mu_s)/\bar{L}_p$, whilst when $\bar{L}_p \leqslant 1$ the system evolves over the dimensional time scale $t \sim H^2/K/(\lambda_s + 2\mu_s)$. Using the parameter values given in §3.2, the model suggests that tissue swelling due to a damaged BBB should evolve over a duration of $t \sim H^2/K/(\lambda_s + 2\mu_s)/\bar{L}_p = 10^2 - 10^4$ s (1 min−1 hour). However, in physiological conditions maximal swelling is observed to develop over the duration of days (Hatashita et al., 1988; Marmarou et al., 2000). Since the time scale for physical changes predicted by the model is much more rapid than that observed biologically, we conclude that the rate of swelling is governed by biological processes (such as the rate at which the BBB becomes permeable) rather than physical processes. As it appears that this biphasic approach is unable to offer insight into the rate of swelling, we neglect dynamics for the remainder of this paper, and instead focus on the steady state equations for tissue in a final damaged equilibrium state.

4. BBB failure in a local region of tissue

We now present solutions to the biphasic model in a sphere. We consider the effect of a local damaged region on the tissue and simulate a local region of damage towards the centre of the tissue by imposing a step function behaviour for $\bar{L}_p(R)$:

$$\bar{L}_p(R) = \begin{cases} 10 & R < 0.2, \\ 0.1 & R > 0.2. \end{cases} \tag{4.1}$$

These parameter values are chosen to reflect capillary hydraulic conductivity in tissue with a central region of BBB damage, surrounded by healthy tissue (see Table 2).

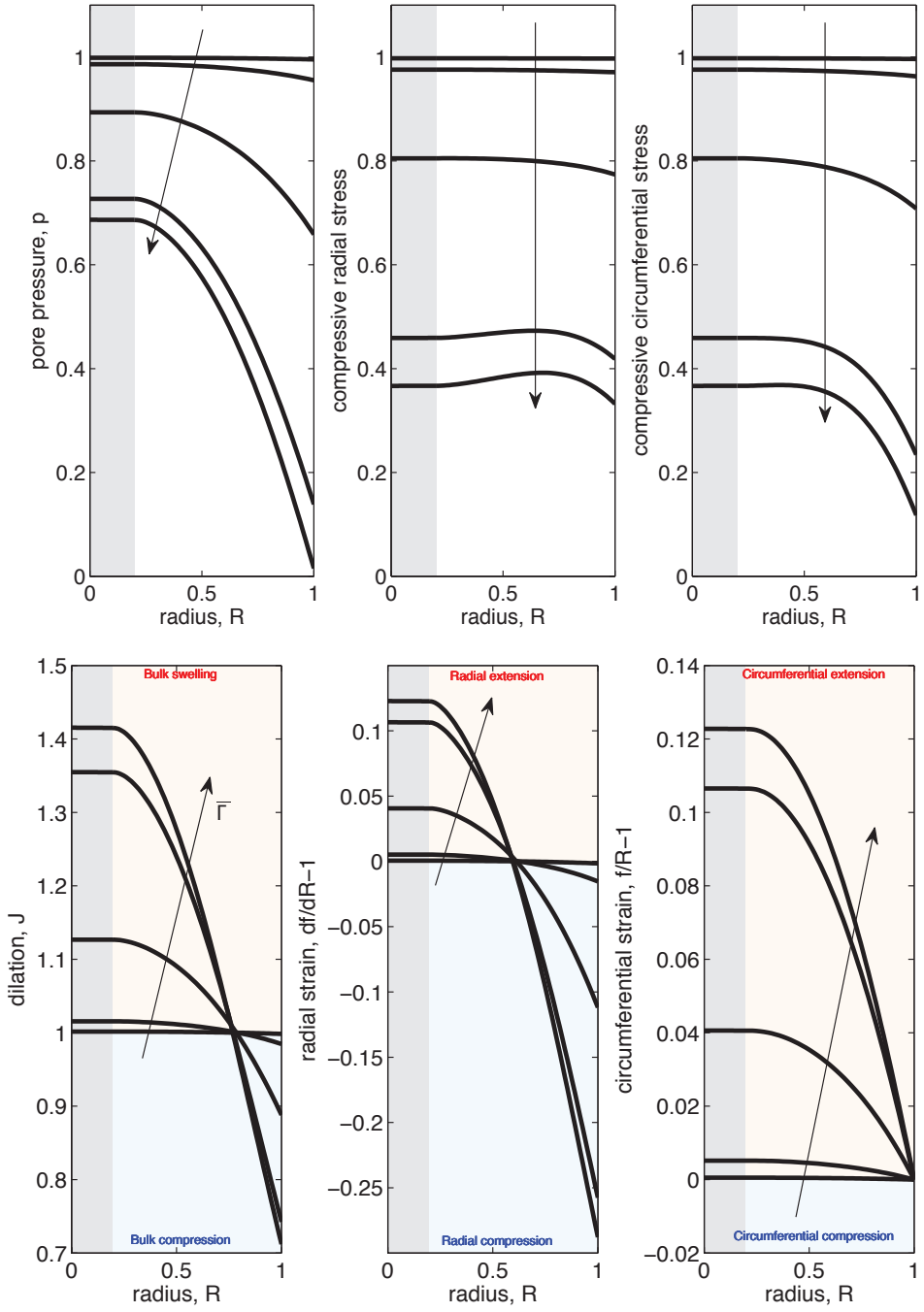

FIG. 3. Solution profiles for the biphasic model with a local region of damage at the centre. Top row shows dilation ($J = f^2 f'/R^2$), radial strain ($f' - 1$) and circumferential strain ($f/R - 1$), whilst bottom row shows pore pressure (p), radial compressive stress ($-\mathbf{e}_r \cdot \boldsymbol{\sigma} \cdot \mathbf{e}_r$), and circumferential compressive stress ($-\mathbf{e}_\theta \cdot \boldsymbol{\sigma} \cdot \mathbf{e}_\theta$). Curves show profiles for tissue which has a damaged BBB towards the centre, so that capillary permeability is $\bar{L}_p$=10 for $0 < R < 0.2$ (grey shaded region), and $\bar{L}_p$=0.1 for $0.2 < R < 1$. Each curve corresponds to a particular value of $\bar{\Gamma}$=0.01, 0.1, 1, 10, 100, with the arrows in the direction of increasing $\bar{\Gamma}$. Other parameters are: $\bar{Y} = 1$, $\bar{\lambda}_s = 0.5$, $\bar{\mu}_s = 0.25$. The light blue region in the bottom row denotes compressive (negative) stress and the light brown region denotes tensile (positive) stress.

4.1 *Steady-state governing equations*

For the finite-deformation governing equations, we substitute the spherically symmetric deformation gradient tensor (2.18) into the Lagrangian form of the governing equation (3.5), and use standard spherical vector operators (Ogden, 1984). We then obtain the following equation for mass conservation at steady state,

$$-\frac{1}{J}\frac{1}{R^2}\frac{\partial}{\partial R}\left(\frac{R^2 J}{f'^2}\frac{\partial p}{\partial R}\right) = \bar{L}_p(R)(\bar{Y}-p). \tag{4.2}$$

Similarly we write the Lagrangian stress balance (3.6)

$$0 = \frac{\mathrm{d}(S_{RR})}{\mathrm{d}R} + \frac{2(S_{RR}-S_{\Theta\Theta})}{R} - \frac{f^2}{R^2}\frac{\mathrm{d}p}{\mathrm{d}R}, \tag{4.3}$$

where S_{RR} and $S_{\Theta\Theta}$ are the diagonal radial and circumferential components of the dimensionless Piola-Kirchhoff stress $\bar{\mathbf{S}}_e$.

Using the strain-energy density (2.11) together with (2.10), the components S_{RR} and $S_{\Theta\Theta}$ required for the stress balance (4.3) may be written as functions of the radial deformation $f(R)$:

$$S_{RR} = \frac{1}{f'}\left[\bar{\mu}_s(f'^2-1) + \bar{\lambda}_s J(J-1)\right], \tag{4.4}$$

$$S_{\Theta\Theta} = \frac{R}{f}\left[\bar{\mu}_s\left(\frac{f^2}{R^2}-1\right) + \bar{\lambda}_s J(J-1)\right] \tag{4.5}$$

To solve the steady state governing equations (4.2) and (4.3), along with boundary conditions (3.7) for a step function for $\bar{L}_p(R)$ (4.1), we use a multipoint boundary value problem solver in Matlab (see Lang, 2014, for details of the numerical methods used).

4.2 *Results*

We are interested in two types of damage: 'strain damage', whereby the tissue is stretched (causing mechanical damage to axons), and 'stress damage', whereby the tissue stress compresses the capillary network (leading to reduced blood flow and hypoxia). The value of the parameter $\bar{\Gamma}$ (representing the ease with which fluid can drain out of the tissue region) is unknown, so we are particularly interested to investigate how the value of $\bar{\Gamma}$ affects the type of damage caused.

Whilst the experimental literature typically interprets increased ICP as the cause of capillary compression ('stress damage'), we must consider what this means within a mixture theory modelling framework. In mixture theory the Cauchy stress is additively decomposed as $\boldsymbol{\sigma} = \boldsymbol{\sigma}_e - p\mathbf{I}$, representing the elastic stress and pore pressure respectively. This framework has been used to model edema by Nagashima et al. (1990b), who used the pore pressure p as a measure of tissue damage. However, we believe that the entire mixture stress acts to compress the capillaries, rather than just the component of the stress attributed to the pore pressure. Hence, we assume that the stress causing damage is related to the total (*i.e.* Cauchy) stress $\boldsymbol{\sigma}$.

In Figure 3 we show dilation, radial and circumferential strain, pore pressure and radial and circumferential compressive stress profiles within the tissue. Curves are shown for different values of $\bar{\Gamma}$. The upper row of Figure 3 shows quantities associated with 'strain damage'. We observe that when $\bar{\Gamma}$ is large, so that fluid can easily flow from the tissue, larger strains occur in the tissue. The dilation

profiles show that the inner region experiences bulk swelling ($J > 1$), whilst the outer region is compressed ($J < 1$). However, considering the radial and circumferential strains shows that the entire tissue is stretched circumferentially, whilst the inner region expands and the outer region contracts radially. When $\bar{\Gamma}$ is small, there is little strain in either direction and the tissue experiences little volume change. The results presented in Figure 3 suggests that strain damage to tissue is worsened when fluid can drain easily out of the tissue (*i.e.* for large $\bar{\Gamma}$.).

The lower row of Figure 3 concerns quantities associated with 'stress damage'. Note in particular that we have plotted the **compressive** radial and circumferential Cauchy stresses (corresponding to $-\mathbf{e}_r \cdot \boldsymbol{\sigma} \cdot \mathbf{e}_r$ and $-\mathbf{e}_\theta \cdot \boldsymbol{\sigma} \cdot \mathbf{e}_\theta$, respectively). Regardless of the value of $\bar{\Gamma}$, we observe that pore pressure approaches the driving pressure $\bar{Y}$ (set equal to 1 in these simulations) in the centre of the tissue. However, we observe that when $\bar{\Gamma}$ is smaller, the compressive stress experienced by the tissue is greater than when $\bar{\Gamma}$ is larger. This suggests that fluid being unable to escape from the tissue may lead to an increase in the 'stress damage' experienced by the tissue. We note that this spherically symmetric geometry does not lead to shear stresses, which are also associated with damage to brain tissue (Zhang et al., 2004).

The results presented in Figure 3 suggest that there is a non-trivial balance between the stress and

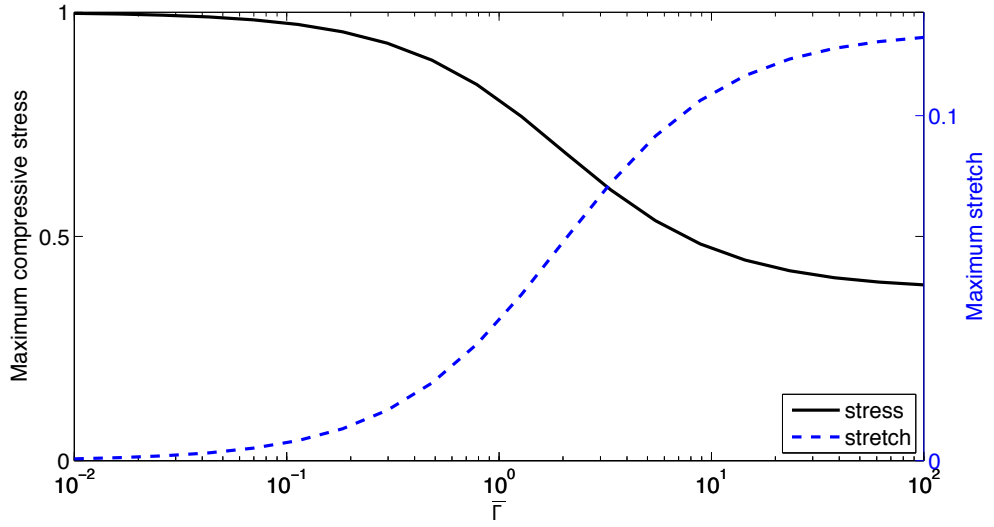

FIG. 4. Maximum compressive stress (black solid curve, left axis) and maximum stretch (blue dashed curve, right axis) experienced by the peripheral tissue ($0.2 < R < 1$), as a function of $\bar{\Gamma}$. All parameters as in Figure 3.

strain distributions in the tissue. Figure 4 shows the maximum compressive stress and maximum strain occurring in the peripheral tissue with intact BBB ($0.2 < R < 1$), as functions of $\bar{\Gamma}$. If $\bar{\Gamma}$ is large, the peripheral tissue is subjected to large strains (due to pressure gradients throughout the tissue), yet the overall compressive stress experienced by the tissue is small. If $\bar{\Gamma}$ is small (so fluid cannot easily escape from the tissue), then the peripheral tissue undergoes little strain (as pressure gradients are small), yet the compressive stress is high everywhere. Thus a local increase in capillary permeability could lead to peripheral tissue experiencing 'stress damage' or 'strain damage', with the type of damage occurring depending on how fluid drains from the system.

5. Discussion

We have used a biphasic modelling approach to investigate how changes in BBB permeability can lead to edema. Whilst we have used a simpler geometry than previous modelling attempts (Nagashima et al., 1990b), we are able to offer new insight into the role of key system parameters. In particular, the dimensionless parameter $\bar{L}_p = L_p H^2/K$, representing the ease with which fluid can flow out of a capillary versus the ease with which fluid can permeate a distance H through the brain, modifies the behaviour of the system. Physiological parameter values indicate that healthy brain tissue (with an intact BBB) operates in the regime $\bar{L}_p < 1$ whilst damaged brain tissue (with a more permeable BBB) operates in the regime $\bar{L}_p > 1$.

Dimensional analysis of the model suggests that when $\bar{L}_p \ll 1$ the pore pressure in the tissue remains low, whilst when $\bar{L}_p \gg 1$ the pore pressure can increase up to the capillary driving pressure. This observation offers an interesting insight into how changes in BBB permeability alone can lead to edema. Furthermore, through dimensional analysis we have shown that the timescale for swelling predicted by the model is more rapid than the timescale of edema formation observed experimentally. This suggests that the rate of edema formation is determined by biological factors beyond the scope of this model (such as the rate of breakdown of the BBB), rather than by mechanical factors alone.

We considered steady-state solutions for a spherical tissue, with an inner region in which the BBB is damaged ($\bar{L}_p > 1$), and an outer, healthy region ($\bar{L}_p < 1$). Our focus here was on the consequences of a locally damaged region of tissue for the surrounding, initially healthy, tissue. We found that where fluid was able to flow freely out of the tissue at the outer boundary (*i.e* large values of the parameter $\bar{\Gamma}$), large pressure gradients and strains were observed within the surrounding healthy tissue. However, where fluid flux out of the tissue at the outer boundary was limited (low $\bar{\Gamma}$), the surrounding healthy tissue experienced high compressive stress (although the strains in the tissue remained low). This indicates that a local increase in capillary permeability can cause damage in surrounding healthy tissue, since both high stresses (which restrict blood flow) and deformations (which cause mechanical damage to axons) may be experienced. Whether it is the compressive stress or the radial stretch that is large influences the type of damage that is observed (Lang et al., 2015) and potentially has clinical implications.

We investigated results for a range of values of $\bar{\Gamma}$, because it is unclear which values of $\bar{\Gamma}$ are physiologically relevant. Furthermore there is some uncertainty in the biological literature as to the mechanisms of CSF absorption in the brain, and how these mechanisms are affected by edema. Future theoretical work could include incorporating a local region of BBB damage into a spherically symmetric or realistic geometry of the entire brain and cerebrospinal fluid system. For example, Smillie et al. (2005) proposed mass conservation boundary conditions for cerebrospinal fluid in the ventricle and subarachnoid space compartments, accounting for pressure-dependent reabsorption of cerebrospinal fluid back into the blood stream. Such an approach would couple the drainage of edema fluid together with other fluid networks within the brain, and offer initial insights into whether 'stress damage' or 'stretch damage' would dominate in reality.

Experimentally, an important contribution would be to estimate the order of magnitude of the parameter Γ. Armed with this information, it would be possible to test the predictions of the model presented here by measuring the stretch caused by a given amount of damage (cf figure 4). An interesting prediction of our model, that may be amenable to experimental confirmation, is that as the value of $\bar{\Gamma} = \Gamma H/K$ changes (for fixed extent of damage) the type of damage observed should also change. In particular, keeping the values of Γ, K and the relative amount damage fixed, our model predicts that the dominant mechanism of damage will alter from stress damage to stretch damage as H increases.

In using the form $Q = L_p(Y - p)$ for the source term for fluid transport from capillaries, we made

two major assumptions. Firstly, we assumed that the transvascular driving pressure Y is constant, and thereby that the capillary pressure and osmotic pressure difference across the BBB remains constant. In fact, the brain has an auto-regulation mechanism for blood flow, and is able to maintain flow to the brain over a range of intracranial pressures; therefore pressure in the vascular system may change during the onset of swelling. Additionally, increases in osmotic pressure of the brain tissue are observed during swelling. Although we have neglected these features in our model, an advantage of our simplistic approach is that we are able to offer a clear insight into the parameters governing the behaviour of the model: when capillary permeability L_p is high the tissue pressure can increase up to the capillary driving pressure Y, whilst when capillary permeability is low the system is less sensitive to this parameter.

Our second major assumption is that there is always enough fluid in the capillaries to allow the capillaries to act as a fluid source. If the compressive stresses in the tissue approach the capillary pressure, we might expect that capillaries become compressed and hence less fluid is available in the capillaries to enter the tissue. As discussed in §1.2, a danger of increased intracranial pressure is a reduction in blood flow. To explicitly model this effect, the capillary network could be modelled as a further fluid phase (using the multi network poroelastic approach of Tully and Ventikos, 2011, for example), or the form of the transvascular fluid source (2.16) could be adapted to allow capillaries to close if they experience high compressive stress.

In the brain, changes in tissue osmolarity are observed alongside edema (Kawamata et al., 2007). Throughout this work we have neglected osmotic effects, by encapsulating the osmotic pressure difference between capillary and brain in the transvascular driving pressure parameter Y. Analysis of our mathematical model indicates that when the BBB is highly permeable ($\bar{L}_p > 1$), the model is sensitive to Y; this suggests that inclusion of osmotic effects is important to gain a better understanding of brain edema. Nevertheless, the present study provides a general conceptual framework to understand the role of BBB permeability in edema formation.

The goal of our paper has been to understand how a localised initial injury can result in mechanical damage beyond the original injury site. We have not considered an anatomically accurate model for the brain, which accounts for realistic geometry, the presence of structures such as the CSF-filled ventricles, or differences in permeability between regions of the brain. Rather, we have demonstrated that localised changes in permeability can indeed result in brain tissue swelling, and the type of damage that results (stress damage or strain damage) depends on the ability of the brain to clear edema fluid. The framework we have developed could, in the future, include regional variations in permeability very easily, and this would be an exciting extension of this work, especially when considering an anatomically realistic model (Lang et al., 2015).

A. Role of dynamics

In this Appendix we consider a time-dependent model for swelling of a biphasic sphere, with constant capillary permeability $\bar{L}_p$ throughout. We are particularly interested in understanding the timescales that govern the behaviour of the system, because maximal edema is observed to occur after several days (Hatashita et al., 1988; Marmarou et al., 2000). If the model predicts that dynamic swelling should occur over a shorter timescale, this would indicate that the dynamics must instead be governed by biological processes beyond the scope of our model.

We work with an infinitesimal deformation model. This simplifies the governing equations, allowing us to focus on the dynamic evolution. In an infinitesimal elasticity framework, the Lagrangian ($\mathbf{X}$) and Eulerian ($\mathbf{x}$) co-ordinate systems are equivalent. The dimensionless governing equations (3.5) and (3.6)

reduce to a coupled system for the radial displacement $u = \mathbf{u} \cdot \mathbf{e}_r$ and pore pressure p,

$$\frac{\partial}{\partial t}(\nabla \cdot \mathbf{u}) - \nabla^2 p = \bar{L}_p (\bar{Y} - p), \tag{A.1}$$

$$\nabla p = \nabla \cdot \left[\bar{\lambda}_s \mathrm{tr}(\mathbf{e}) + 2\bar{\mu}_s \mathbf{e}\right] \tag{A.2}$$

where $\mathbf{e} = [\nabla \mathbf{u} + (\nabla \mathbf{u})^T]/2$ is the linear strain tensor, and we have substituted the infinitesimal stress tensor $\bar{\boldsymbol{\sigma}}_e = \bar{\lambda}_s \mathrm{tr}(\mathbf{e})\mathbf{I} + 2\bar{\mu}_s \mathbf{e}$ into the stress balance (A.2). We define $e = \mathrm{tr}(\mathbf{e}) = \nabla \cdot \mathbf{u}$ as a measure of the local strain.

We impose the initial conditions that both pressure and displacement are zero initially ($u(r,0)$=0, $p(r,0)$=0). We choose the specific case $1/\bar{\Gamma} = 0$ for our boundary condition on the outer edge (3.7) (meaning that there is no resistance to fluid flow through the outer boundary), so that $u = 0$, $p = 0$ at $r = 1$, along with symmetry at the origin (2.22). (In §4.2 we investigate the effect of varying $\bar{\Gamma}$ in the finite deformation model.) We choose these simple boundary and initial conditions to gain insight into the behaviour of the system. Trivially, it can be observed that if $\bar{L}_p = 0$ (*i.e.* the capillaries are completely impermeable to water) then $p = 0$, $u = 0$ is a solution that satisfies the specified boundary conditions. Therefore the set up we consider corresponds to undeformed tissue undergoing an instantaneous increase in capillary permeability at time $t = 0$.

From the dimensionless governing equations, we now identify the appropriate early and late time behaviours.

A.1 *Early times*

The initial conditions ($p = 0$, $u = 0$) indicate that for early times, the pressure and displacement are both small. This motivates the scalings,

$$t = \varepsilon \hat{t}, \qquad p = \varepsilon \hat{p}, \qquad \mathbf{u} = \varepsilon \hat{\mathbf{u}}, \tag{A.3}$$

for some $\varepsilon \ll 1$ where $\hat{t}$, $\hat{p}$, $\hat{\mathbf{u}}$ are early time variables. Then the mass conservation governing equation may be written,

$$\frac{\partial}{\partial \hat{t}}(\nabla \cdot \hat{\mathbf{u}}) - \varepsilon \nabla^2 \hat{p} = \bar{L}_p (\bar{Y} - \varepsilon \hat{p}). \tag{A.4}$$

Since $\varepsilon \ll 1$ the strain $e = \nabla \cdot \hat{\mathbf{u}}$ will increase at a constant rate, $\bar{L}_p \bar{Y}$, and so,

$$\nabla \cdot \hat{\mathbf{u}} = \bar{L}_p \bar{Y} \hat{t} \tag{A.5}$$

for $t \ll 1$, where we have used $\hat{\mathbf{u}} = \mathbf{0}$ at $t = 0$ to eliminate a constant of integration. The corresponding pressure is found by solving equation (A.2).

A.2 *Late times*

At late times, the system reaches a steady state. The time taken for the system to reach this steady state depends on the parameter regime of the system. The dimensionless parameter $\bar{L}_p = L_p H^2/K$ represents the ratio of the ease with which fluid can enter the tissue from the capillary, relative to the ease with which fluid can drain out through the tissue a distance H to the boundary. We consider in particular the limits $\bar{L}_p \ll 1$ and $\bar{L}_p \gg 1$.

$\bar{L}_p \ll 1$

When $\bar{L}_p \ll 1$, the mixture is sufficiently permeable that water is able to drain out of the system at pressures below the capillary driving pressure $\bar{Y}$. Thus we anticipate a dominant balance between the source of fluid entering from capillaries, and fluid drainage out through the tissue at steady state. We scale for late times,

$$t = \tilde{t}, \qquad p = \bar{L}_p \bar{Y} \tilde{p}, \qquad \mathbf{u} = \bar{L}_p \bar{Y} \tilde{\mathbf{u}}, \tag{A.6}$$

where $\tilde{t}$, $\tilde{p}$, $\tilde{u}$ are late time variables and find,

$$\frac{\partial}{\partial \tilde{t}} (\nabla \cdot \tilde{\mathbf{u}}) - \nabla^2 \tilde{p} = 1 - \bar{L}_p \tilde{p}. \tag{A.7}$$

Since $\bar{L}_p \ll 1$, this indicates that we can neglect the last term in (A.7) and the dominant balance is indeed between the flux of fluid draining out of the system (the $\nabla^2 \tilde{p}$ term) and fluid entering the system from capillaries as anticipated. The pressure in the system will be of order $\bar{L}_p \bar{Y}$. Furthermore, we expect the system to evolve over an order 1 timescale, independent of $\bar{L}_p$.

$\bar{L}_p \gg 1$

When $\bar{L}_p \gg 1$ we expect the pressure to approach the capillary driving pressure $\bar{Y}$, as we anticipate that at steady state the dominant balance in the mass conservation equation (A.1) will be between the two terms on the RHS. We instead scale for late time variables to reflect this expectation,

$$t = \bar{L}_p^{-1} \tilde{t}, \qquad p = \bar{Y} \tilde{p}, \qquad \mathbf{u} = \bar{Y} \tilde{\mathbf{u}}, \tag{A.8}$$

so that

$$\frac{\partial}{\partial \tilde{t}} (\nabla \cdot \tilde{\mathbf{u}}) - \frac{1}{\bar{L}_p} \nabla^2 \tilde{p} = 1 - \tilde{p}. \tag{A.9}$$

Since $\bar{L}_p \gg 1$, at steady state the dominant balance in the above equation is between the terms on the right hand side. This implies that $\tilde{p} \approx 1$ (*i.e* $p \approx \bar{Y}$) at steady state. Furthermore, the time scaling indicates that the time taken for the system to reach equilibrium is proportional to $1/\bar{L}_p$.

A.3 *Validation of dimensional analysis*

We now solve the fully time-dependent biphasic problem (A.1)-(A.2) numerically, and compare these numerical results to the predictions for the rate of evolution of the system from our dimensional analysis. In a spherically symmetric geometry, equations (A.1)-(A.2) may be rewritten,

$$(\bar{\lambda}_s + 2\bar{\mu}_s) \frac{\partial}{\partial r} \left(\frac{1}{r^2} \frac{\partial}{\partial r} \left(r^2 u \right) \right) = \frac{\partial p}{\partial r}, \tag{A.10}$$

$$\frac{\partial}{\partial t} \left(\frac{1}{r^2} \frac{\partial}{\partial r} \left(r^2 u \right) \right) - \frac{1}{r^2} \frac{\partial}{\partial r} \left(r^2 \frac{\partial p}{\partial r} \right) = \bar{L_p} \left[\bar{Y} - p \right]. \tag{A.11}$$

where $u = \mathbf{u} \cdot \mathbf{e}_r$ is the radial displacement. We solve equations (A.10)-(A.11), subject to initial conditions $p(r,0)$=0 and $u(r,0)$=0, and boundary conditions $p(t,1)$=0, $u(t,1)$=0, numerically using the

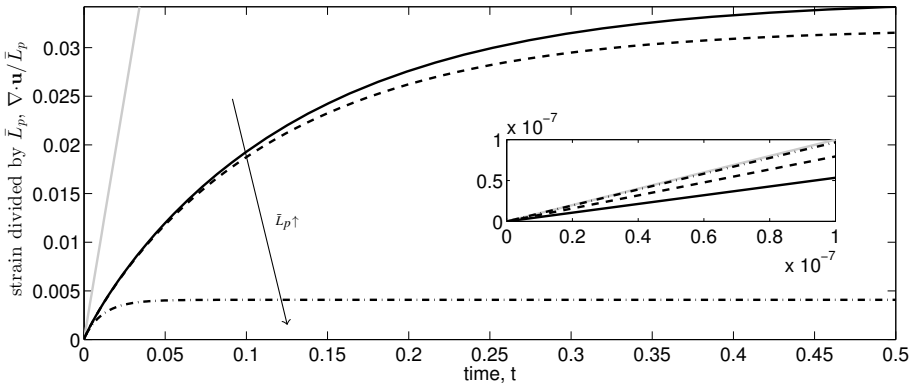

FIG. 5. Black curves: strain scaled by $\bar{L}_p$, $\nabla\cdot\mathbf{u}/\bar{L}_p$, against time for a biphasic model with capillary source in a spherical geometry. The strain shown is at the centre of the sphere. Grey lines are $\bar{Y}t$, and the inset figures show that for very early times strain satisfies (A.5). Parameter values are: $\bar{\lambda}_s = 0.5$, $\bar{\mu}_s = 0.25$, $\bar{Y} = 1$, and curves are shown for $\bar{L}_p = 0.01$ (solid), $\bar{L}_p = 1$ (dashed) and $\bar{L}_p = 100$ (dot-dashed) with the arrow in direction of increasing $\bar{L}_p$. For each of these simulations the domain [0, 1] was discretised into $N = 100$ gridpoints and the system was solved using the Method of Lines, as described in Section A.3.

Method of Lines. We discretise each governing equation in space using a second-order central finite difference method. This results in a system of differential algebraic equations, which can be solved using the Matlab solver 'ode15s'.

In Figure 5 we show numerical results for the evolution of strain (at the centre of a sphere), for three different values of $\bar{L}_p$. The inset shows that in each case the strain initially increases linearly with time, with slope $\bar{L}_p\bar{Y}$. When $\bar{L}_p = 1$ and $\bar{L}_p = 0.01$ the time taken for the system to evolve to steady state equilibrium is similar, whilst for $\bar{L}_p = 100$ the system evolves to equilibrium very rapidly.

We now test our assertion that if $\bar{L}_p \ll 1$ then the time taken for the system to evolve to equilibrium is of order 1 independent of $\bar{L}_p$, whilst if $\bar{L}_p \gg 1$ then the time taken to evolve to equilibrium is of order $1/\bar{L}_p$. Figure 6 shows the time taken for the pressure (at the centre of a sphere) to reach within $1/e$ of its equilibrium value, t_{ss}. As expected, we observe that when $\bar{L}_p \ll 1$, t_{ss}=constant, whilst when $\bar{L}_p \gg 1$ then $t_{ss} \sim 1/\bar{L}_p$.

The relevance of these findings to the development of brain edema, along with relevant parameter values, are discussed in §3.3.

B. Role of nonlinear deformations

Previous authors have used a similar biphasic modelling approach to investigate the mechanical behaviour of brain tissue (Nagashima et al., 1990b; Smith and Humphrey, 2007), although a model valid for only infinitesimal deformations was used. In this Appendix, we compare the difference in steady-state stress and strain profiles obtained when using an infinitesimal vs. finite deformation model.

We use a step function for the capillary permeability (4.1), to represent a local damaged region in the centre of the tissue, which therefore has increased capillary permeability. For the finite deformation model, the governing equations are given by equations (4.2) and (4.3), along with boundary conditions (3.7) at the origin and at the tissue boundary. For the infinitesimal deformation model, the governing

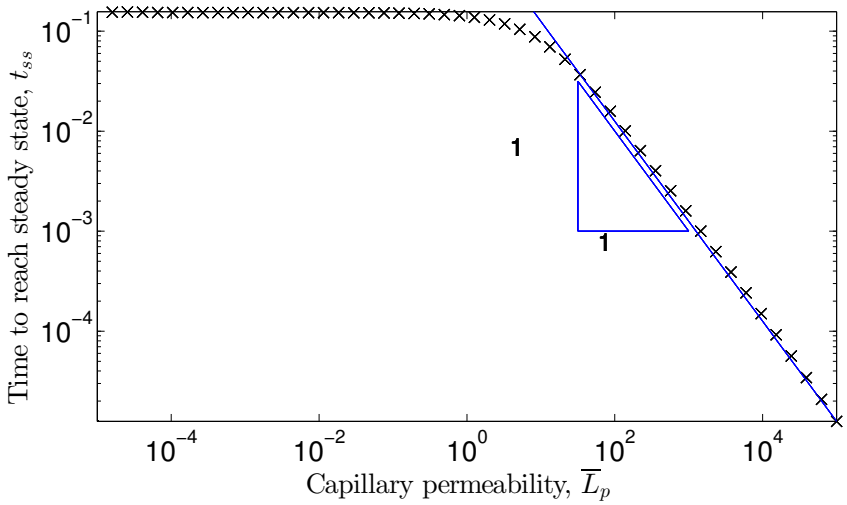

FIG. 6. Plot showing the time taken for the pressure of a biphasic system to reach within $1/e$ of its steady state value, t_{ss}, as a function of the dimensionless capillary permeability $\bar{L}_p$. The crosses show results of these numerical simulations, whilst the solid line shows a line of best fit satisfying the expected scaling $t_{ss} \sim 1/\bar{L}_p$ for $\bar{L}_p \gg 1$; in particular, $t_{ss} = 1.25/\bar{L}_p$.

equations are (A.10) and (A.11) in steady state, along with boundary conditions,

$$u|_0 = 0, \qquad \left.\frac{\mathrm{d}p}{\mathrm{d}r}\right|_1 = \bar{\Gamma} p|_1 \tag{B.1}$$

In Figure 7, we compare profiles for the radial and compressive stretch and compressive stress through the tissue, obtained using the infinitesimal and finite deformation models. We observe that whilst the results show quantitatively different behaviour, qualitatively the behaviour is similar. This suggests that despite strains of greater than 5% (typically assumed to be the greatest strains for which the infinitesimal model is valid), the infinitesimal theory can still offer insight into the behaviour of the tissue.

References

N. J. Abbott. Evidence for bulk flow of brain interstitial fluid: significance for physiology and pathology. *Neurochemistry International*, 45(4):545 – 552, 2004. ISSN 0197-0186. doi: http://dx.doi.org/10.1016/j.neuint.2003.11.006.

N. J. Abbott, L. Rönnbäck, and E. Hansson. Astrocyte-endothelial interactions at the blood-brain barrier. *Nat. Rev. Neurosci.*, 7:41–53, 2006.

N. J. Abbott, A. A. K. Patabendige, D. E. M. Dolman, S. R. Yusof, and D. J. Begley. Structure and function of the blood-brain barrier. *Neurobio. Dis.*, 37:1325, 2010.

E. N. T. Bakker, B. J. Bacskai, M. Arbel-Ornath, R. Aldea, B. Bedussi, A. W. J. Morris, R. O. Weller, and R. O. Carere. Lymphatic clearance of the brain: perivascular, paravascular and significance for neurodegenerative diseases. *Cell. Mol. Neurobiol.*, 2016. doi: 10.1007/s10571-015-1273-8

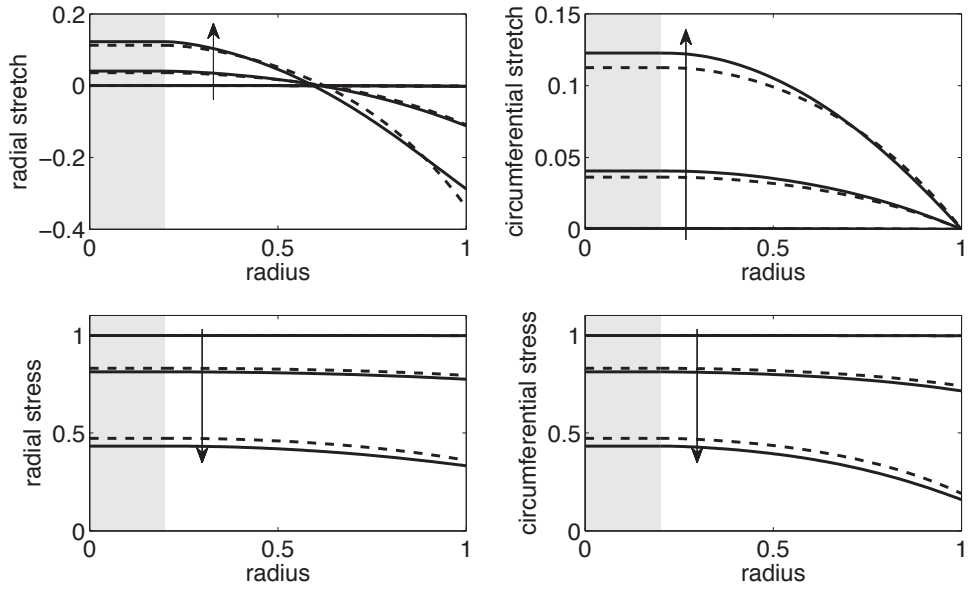

FIG. 7. Profiles of stretch and compressive stress calculated using the finite deformation (solid curves) and infinitesimal deformation (dashed curves) models, for $\bar{\Gamma} = 0.01, 1, 100$ (arrow in direction of increasing $\bar{\Gamma}$). Profiles are shown for radial and circumferential stretch and stress, as these are the measures that we use as a proxy for tissue damage. We observe that the finite and infinitesimal models display qualitatively similar behaviour for all values of $\bar{\Gamma}$. Parameters: $\bar{Y} = 1$, $\bar{\lambda}_s = 0.5$, $\bar{\mu}_s = 0.25$.

M. W. Bradbury. The blood-brain barrier. transport across the cerebral endothelium. *Circulation research*, 57(2):213–222, 1985.

X. Chen and M. Sarntinoranont. Biphasic finite element model of solute transport for direct infusion into nervous tissue. *Ann. Biomed. Eng.*, 35(12):2145–2158, 2007.

L. T. Dunn. Raised intracranial pressure. *Journal of Neurology, Neurosurgery & Psychiatry*, 73(suppl 1):i23–i27, 2002. doi: 10.1136/jnnp.73.suppl_1.i23.

C. J. Ek, K. M. Dziegielewska and N. R. Saunders. Development of the blood-cerebrospinal fluid barrier. In: The blood-cerebrospinal fluid barrier, edited by W. Zheng and A. Chodobski, 3-23, 2005.

B. S. Elkin, M. A. Shaik, and B. Morrison III. Fixed negative charge and the Donnan effect: A description of the driving forces associated with brain tissue swelling and edema. *Phil. Trans. Royal Soc. London A*, 368(1912):585–603., 2010. doi: 10.1098/rsta.2009.0223.

J. Flechsenhar, J. Woitzik, K. Zweckberger, H. Amiri, W. Hacke, and E. Jüttler. Hemicraniectomy in the management of space-occupying ischemic stroke. *J. Clin. Neurosci.*, 20(1):6–12, 2013.

J. J. García and J. H. Smith. A biphasic hyperelastic model for hydrocephalus. *Lat. Am. appl. res.*, 40(4):295–302, 2010.

J. J. García and J. H. Smith. A biphasic hyperelastic model for the analysis of fluid and mass transport in brain tissue. *Ann. Biomed. Eng.*, 37:375–386, 2009. ISSN 0090-6964. doi: 10.1007/s10439-008-9610-0.

T. Gerriets, E. Stolz, M. Walberer, C. Müller, A. Kluge, A. Bachmann, M. Fisher, M. Kaps, and G. Bachmann. Noninvasive quantification of brain edema and the space-occupying effect in rat stroke models using magnetic resonance imaging. *Stroke*, 35:566–571, 2004. doi: 10.1161/01.STR.0000113692.38574.57.

A. Goriely, J.A. W. van Dommelen, M. G. D. Geers, G. Holzapfel, J. Jayamohan, A. Jérusalem, S/.Sivaloganathan, W. Squier, S. Waters, E. Kuhl. Mechanics of the Brain: Perspectives, Challenges, and Opportunities. *Biomed. Model. Mechanobiol.* (in press), 2015. doi: 10.1007/s10237-015-0662-4

S. Hatashita, J. T. Hoff, and S. M. Salamat. Ischemic brain edema and the osmotic gradient between blood and brain. *J. Cereb. Blood Flow Metab.*, 8(4):525–559, 1988. doi: 10.1038/jcbfm.1988.96.

M. H. Holmes. A theoretical analysis for determining the nonlinear hydraulic permeability of a soft tissue from a permeation experiment. *Bull. Math. Biol.*, 47(5):669–683, 1985.

N. A. Jessen, A. S. F. Munk, I. Lundgaar, and M. Nedergaard. The glymphatic system: a beginner's guide. *Neurochem. Res.*, 2015. doi: 10.1007/s11064-015-1581-6

C. E. Johanson. Choroid plexus cerebrospinal fluid circulatory dynamics: Impact on brain growth, metabolism, and repair. In P. Michael Conn, editor, *Neuroscience in Medicine*, pages 173–200. Humana Press, 2008.

T. Kawamata, T. Mori, S. Sato, and Y. Katayama. Tissue hyperosmolality and brain edema in cerebral contusion. *Neurosurg. Focus*, 22(5):1–8, 2007. doi: 10.3171/foc.2007.22.5.6.

H. K. Kimelberg. Current concepts of brain edema: Review of laboratory investigations. *J. Neurosurg.*, 83:10511059, 1995. doi: 10.3171/jns.1995.83.6.1051.

R. Korthuis, J. Scallan, and V. Huxley. *Capillary Fluid Exchange: Regulation, Functions, and Pathology*. Morgan Claypool Publishers, 2010.

G. E. Lang. *Mechanics of swelling and damage in brain tissue: a theoretical approach*. PhD thesis, University of Oxford, 2014. `http://ora.ox.ac.uk/objects/uuid:7a82de9b-adc0-4160-9b6e-fbf748f1dea2`

G. E. Lang, P. S. Stewart, D. Vella, S. L. Waters, and A. Goriely. Is the Donnan effect sufficient to explain swelling in brain tissue slices? *J. R. Soc. Interface*, 11(96), 2014. doi: 10.1098/rsif.2014.0123.

G. E. Lang, D. Vella, S. L. Waters, and A. Goriely. Propagation of damage in brain tissue: Coupling the mechanics of edema and oxygen delivery. *Biomed. Model. Mechanobiol.* 14, 1197–1216, 2015. doi: 0.1007/s10237-015-0665-1

A. Louveau, I. Smirnov, T. J. Keyes, J. D. Eccles, S. J. Rouhani, J. D. Peske, N. C. Derecki, D. Castle, J. W. Mandell, K. S. Less, T. H. Harris, and J. Kipnis. Structural and functional features of central nervous system lymphatic vessels. *Nature*, 523, 337–341, 2015.

A. F. Mak, W. M. Lai, and V. C. Mow. Biphasic indentation of articular cartilage. I: Theoretical analysis. *J. Biomech.*, 20(7):703 – 714, 1987.

A. Marmarou, P. P. Fatouros, P. Barzó, G. Portella, M. Yoshihara, O. Tsuji, T. Yamamoto, F. Laine, S. Signoretti, J. D. Ward, M. R. Bullock, and H. F. Young. Contribution of edema and cerebral blood volume to traumatic brain swelling in head-injured patients. *J. Neurosurg.*, 93(2):183–193, 2000. doi: 10.3171/jns.2000.93.2.0183.

R. Moran, J.H.Smith, and J.J.Garcia. Fitted hyper elastic parameters for Human brain tissue from reported tension, compression, and shear tests. *J. Biomech.* 47:3762–3766, 2014. doi: doi:10.1016/j.jbiomech.2014.09.030

T. Nagashima, B. Horwitz, and S. L. Rapoport. A mathematical model for vasogenic brain edema. *Adv. Neurol.*, 52, 327-26, (1990)

T. Nagashima, T. Shirakuni, and S. I. Rapoport. A two-dimensional, finite element analysis of vasogenic brain edema. *Neurol. Med. Chir.*, 30(1):1, 1990. doi: 10.2176/nmc.30.1.

J. Neal, M. Takahashi, M. Silva, G. Tiao, C. A. Walsh and V. L. Sheen. Insights into the gyrification of developing ferret brain by magnetic resonance imaging. *J. Anat.*, 210 (1), 66–77, 2007.

R. W. Ogden. *Non Linear Elastic Deformations*. Ellis-Horwood, 1984.

A. Raslan and A. Bhardwaj. Medical management of cerebral edema. *Neurosurg. Focus*, 22(5):1–12, 2007. doi: 10.3171/foc.2007.22.5.13.

S. I. Rapoport. A mathematical model for vasogenic brain edema. *J. Theor. Biol.*, 74(3):439–467, 1978.

S. I. Rapoport. 7 - brain edema and the blood-brain barrier. In *Primer on Cerebrovascular Diseases*, pages 25 – 28. Academic Press, San Diego, 1997. ISBN 978-0-12-743170-3. doi: http://dx.doi.org/10.1016/B978-012743170-3.50008-X.

Z. B. Redzic, J. E. Preston, J. A. Duncan, A. Chodobski, and J. Szmydynger-Chodobska. The choroid plexus–cerebrospinal fluid system: From development to aging. *Curr. Top. Dev. Biol.*, 71:1–52, 2005. doi: 10.1016/S0070-2153(05)71001-2.

H. J. Reulen, R. Graham, M. Spatz, and I. Klatzo. Role of pressure gradients and bulk flow in dynamics of vasogenic brain edema. *J. Neurosurg.*, 46(1):24–35, 1977. doi: 10.3171/jns.1977.46.1.0024.

J. M. Simard, T. A. Kent, M. Chen, K. V. Tarasov, and V. Gerzanich. Brain oedema in focal ischaemia: molecular pathophysiology and theoretical implications. *Lancet. Neurol.*, 6:258–68, 2007. doi: 10.1016/S1474-4422(07)70055-8.

A. Smillie, I. Sobey, and Z. Molnar. A hydroelastic model of hydrocephalus. *J. Fluid Mech.*, 539: 417–443, 2005. doi: 10.1017/S0022112005005707.

Q. R. Smith. A review of blood-brain barrier transport techniques. In Sukriti Nag, editor, *The Blood-Brain Barrier : Biology and Research Protocols*, pages 193–208. Springer, 2003.

J. H. Smith and J. A. C. Humphrey. Interstitial transport and transvascular fluid exchange during infusion into brain and tumor tissue. *Microvascular research*, 73(1):58–73, 2007. doi: 10.1016/j.mvr.2006.07.001.

D. H. Smith and D. F. Meaney. Axonal damage in traumatic brain injury. *The Neuroscientist*, 6(6): 483–495, 2000. doi: 10.1177/107385840000600611.

I. Sobey, A. Eisenträger, B. Wirth, and M. Czosnyka. Simulation of cerebral infusion tests using a poroelastic model. *Int. J. Numer. Anal. Model., Ser. B*, 3:52–64, 2012.

L. A. Steiner and P. J. D. Andrews. Monitoring the injured brain: ICP and CBF. *British Journal of Anaesthesia*, 97(1):26–38, 2006. doi: 10.1093/bja/ael110.

S. Strandgaard, J. Olesen, E. Skinhøj, and N. A. Lassen. Autoregulation of brain circulation in severe arterial hypertension. *Br Med J.*, 1(5852):507–510., 1973.

M. D. Tang-Schomer, A. R. Patel, P. W. Baas, and D. H. Smith. Mechanical breaking of microtubules in axons during dynamic stretch injury underlies delayed elasticity, microtubule disassembly, and axon degeneration. *The FASEB Journal*, 24(5):1401–1410, 2010.

Z. Taylor and K. Miller. Reassessment of brain elasticity for analysis of biomechanisms of hydrocephalus. *J. Biomech.*, 37(8):1263 – 1269, 2004. ISSN 0021-9290.

R. Thiex and S. E. Tsirka. Brain edema after intracerebral hemorrhage: mechanisms, treatment options, management strategies, and operative indications. *Neurosurg. Focus*, 22(5):1–7, 2007.

B. Tully and Y. Ventikos. Cerebral water transport using multiple-network poroelastic theory: application to normal pressure hydrocephalus. *J. Fluid Mech.*, 667:188–215, 2011. doi: 10.1017/S0022112010004428.

A. W. Unterberg, J. Stover, B. Kress, and K. L. Kiening. Edema and brain trauma. *Neuroscience*, 129 (4):1019 – 1027, 2004.

M. Walberer, N. Ritschel, M. Nedelmann, K. Volk, C. Müller, M. Tschernatsch, E. Stolz, F. Blaes, G. Bachmann, and T. Gerriets. Aggravation of infarct formation by brain swelling in a large territorial stroke: a target for neuroprotection? *J. Neurosurg.*, 109(2):287–293, 2008.

W. Wilson, C. C. van Donkelaar and J. M. Huyghe. A comparison between mechano-electrochemical and biphasic swelling theories for soft hydrated tissues. *J. Biomech. Eng.*, 127, 158–165.

B. Wirth and I. Sobey. An axisymmetric and fully 3D poroelastic model for the evolution of hydrocephalus. *Math. Med. Biol.*, 23(4):363–388, 2006. doi: 10.1093/imammb/dql014.

B. Wirth and I. Sobey. Analytic solution during an infusion test of the linear unsteady poroelastic equations in a spherically symmetric model of the brain. *Math. Med. Biol.*, 26(1):25–61, 2009.

L. Zhang, K. H. Yang, and A. I. King. A proposed injury threshold for mild traumatic brain injury. *J. Biomech. Eng.*, 126(2):226–236, 2004.